

Gravitational-wave inference for eccentric binaries: the argument of periapsis

Teagan A. Clarke^{1,2*}, Isobel M. Romero-Shaw^{1,2,3}, Paul D. Lasky^{1,2} and Eric Thrane^{1,2}

¹*School of Physics and Astronomy, Monash University, VIC 3800, Australia*

²*OzGrav: The ARC Centre of Excellence for Gravitational-wave Discovery, Clayton, VIC 3800, Australia*

³*Department of Applied Mathematics and Theoretical Physics, Cambridge CB3 0WA, United Kingdom*

29 June 2022

ABSTRACT

Gravitational waves from binary black hole mergers have allowed us to directly observe stellar-mass black hole binaries for the first time, and therefore explore their formation channels. One of the ways to infer how a binary system is assembled is by measuring the system’s orbital eccentricity. Current methods of parameter estimation do not include all physical effects of eccentric systems such as spin-induced precession, higher-order modes and the initial argument of periapsis: an angle describing the orientation of the orbital ellipse. We explore how varying the argument of periapsis changes gravitational waveforms and study its effect on the inference of astrophysical parameters. We use the eccentric spin-aligned waveforms TEOBResumS and SEOBNRE to measure the change in the waveforms as the argument of periapsis is changed. We find that the argument of periapsis is likely to be resolvable in the foreseeable future only for the loudest events observed by LIGO–Virgo–KAGRA. The systematic error in previous analyses that have not taken into account the argument of periapsis is likely to be small.

Key words: gravitational waves – stars: black holes – binaries: general – black hole mergers

1 INTRODUCTION

Approximately 90 gravitational-wave events have been detected (Abbott et al. 2021a,b), including two binary neutron star mergers (Abbott et al. 2017; Abbott et al. 2020b), approximately two neutron star-black hole binary mergers (Abbott et al. 2021e) and over 80 binary black hole mergers (Abbott et al. 2019, 2021c; Abbott et al. 2021a). Despite the wealth of observations, the question of how the population of merging compact binaries formed has proved challenging to answer. For stellar-mass binary black holes, there are two overarching formation channels that could result in coalescence within the Hubble time: isolated binary evolution and dynamical assembly (for a recent overview see, e.g., Mandel & Farmer (2022)). A binary black hole formed in isolation undergoes normal binary stellar evolution until both stars collapse into black holes, with no interaction with external objects (e.g., Bethe & Brown 1998; Belczynski et al. 2016; Stevenson et al. 2017). Alternatively, black hole binaries may form via dynamical assembly: both objects have already evolved into black holes, and become gravitationally bound in a densely-populated environment like a globular cluster or galactic nucleus (e.g., O’Leary et al. 2006; Rodriguez et al. 2016; Yang et al. 2019; Gröbner et al. 2020).

Measuring the orbital eccentricity, along with the component masses and spins, of the black holes in a binary can help determine how the binary formed. Since binaries circularise through the emission of gravitational waves (Peters 1964), isolated binaries are expected to have almost circular orbits when they enter the observing band of LIGO–Virgo–KAGRA (LVK) $\approx 10 - 2000$ Hz (Aasi et al.

2015; Acernese et al. 2015; Akutsu et al. 2020). Meanwhile, binaries formed through dynamical assembly can merge very quickly, and hence maintain measurable eccentricity in the LVK observing band (e.g., O’Leary et al. 2009; Rodriguez et al. 2018; Zevin et al. 2021).

Signatures of dynamical formation, such as orbital eccentricity (Romero-Shaw et al. 2019; Lower et al. 2018; Romero-Shaw et al. 2021, 2022; O’Shea & Kumar 2021) and misaligned spins (Abbott et al. 2021d), inferred in some of the existing gravitational-wave observations suggest that dynamically-formed systems may make up a substantial sub-population of binary black holes that merge. However, at least some binaries must be assembled in the field to account for the tendency of LVK binaries to merge with aligned spin (Abbott et al. 2021b). Up to four of the binary black hole mergers observed to date have been identified as potentially eccentric (Romero-Shaw et al. 2019; Wu et al. 2020; Romero-Shaw et al. 2021; O’Shea & Kumar 2021; Romero-Shaw et al. 2022), including the high-mass system, GW190521 (Abbott et al. 2020a; Romero-Shaw et al. 2020b; Gayathri et al. 2022).

While most of the discussion of eccentric binaries has focused on measuring the eccentricity e , the gravitational-wave signal from an eccentric binary is also affected by the argument of periapsis at the reference frequency ω_{ref} . This parameter is the angle of rotation of an elliptical orbit relative to a reference plane, and is one of the 17 parameters that fully describe an eccentric binary black hole system. To illustrate how the argument of periapsis affects gravitational waveforms, we plot in Fig. 1, the gravitational-wave frequency of the dominant ($\ell = 2, |m| = 2$) mode as a function of time for two gravitational waveforms, generated with a difference of π in their reference ω . This change causes the binary to experience periapsis

*teagan.clarke@monash.edu

and apoapsis at different frequencies, despite them having the same eccentricity at 10 Hz.

There are few eccentric waveform approximants available and none currently used for astrophysical inference of LVK data include ω_{ref} as a parameter. The waveform models used to search for eccentricity in the studies above—SEOBNRE (Cao & Han 2017; Yun et al. 2021; Liu et al. 2020), TEOBResumS (Nagar et al. 2018; Nagar et al. 2020; Chiaramello & Nagar 2020) and EccentricFD (Huerta et al. 2014)—do not allow the user to straightforwardly vary ω . However, some new eccentric waveform models are intended to provide this option. Klein (2021) has developed a new waveform model that allows the user to vary ω ; this waveform model has been used to study inference of eccentric binaries with LISA (Buscicchio et al. 2021).

Islam et al. (2021) developed a numerical relativity surrogate waveform with a variable mean anomaly l_{ref} . By simulating equal mass binary, moderately eccentric ($e_{\text{ref}} = 0.1$) waveform predictions with varied l_{ref} in white noise, they found waveform mismatches up to 0.1. This result would seem to suggest that the argument of periapsis has an important effect on the eccentricity measurements obtained using current eccentric waveforms. However, the effect of ω_{ref} on gravitational-wave inference is poorly understood since previous analyses used a fixed value of ω_{ref} , set by the choice of starting eccentricity and reference frequency. Understanding the role of ω_{ref} is important to avoid bias in eccentric parameter estimation. Systematic error related to the argument of periapsis has been assumed to be small, but in light of work by Islam et al. (2021), this assumption must be checked (Lower et al. 2018; Romero-Shaw et al. 2021). In this Paper, we investigate the effect of ω_{ref} on gravitational-wave source inference. In Section 2 we describe the argument of periapsis and our prescription for measuring it in Section 3. In Section 4, we assess the extent to which ω_{ref} can be resolved and discuss the implications of our results.

2 THE EFFECTIVE ARGUMENT OF PERIAPSIS

To investigate the effect of the reference argument of periapsis ω_{ref} on gravitational-wave source inference, we must find a way to change ω_{ref} in the waveform models so that we may measure the effect it has on parameter estimation. Unfortunately, no currently available waveform approximants allow the user to directly control ω_{ref} . Thus, in this section, we devise a mechanism that we can use to vary ω_{ref} indirectly. We use two waveform models for our demonstration: the time-domain effective one-body (Buonanno & Damour 1999) waveform models TEOBResumS (Nagar et al. 2018; Nagar et al. 2020; Chiaramello & Nagar 2020) and SEOBNRE (Cao & Han 2017; Yun et al. 2021; Liu et al. 2020). The eccentric version of TEOBResumS is validated against numerical relativity simulations for eccentricities up to $e \lesssim 0.3$ at 10 Hz for a binary with total mass $60 M_{\odot}$. SEOBNRE is validated up to eccentricities of 0.2 at 10 Hz. Both waveforms are limited to spin-aligned systems.¹

Using these waveforms, ω_{ref} can be indirectly varied by changing the waveform reference frequency f_{ref} , and the eccentricity at f_{ref} , e_{ref} . By setting these waveform parameters, we set an unknown but specific ω_{ref} , which is the argument of periapsis at f_{ref} . The variable

ω_{ref} should change by 2π when the reference frequency and eccentricity have been varied through one orbital period. This means that we can vary ω_{ref} indirectly by following the waveform through a cycle of eccentricity and frequency evolution. The trick is to find the path through $(e_{\text{ref}}, f_{\text{ref}})$ that corresponds to a fixed value of eccentricity at 10 Hz. We call this “the e_{10} path.” Each point along the e_{10} path corresponds to a different value of ω_{ref} .

In order to estimate the e_{10} path, we evolve the orbital eccentricity from f_{ref} back to 10 Hz. To this end we employ a post-Newtonian approximation that describes the eccentricity as a function of gravitational-wave frequency. We use the approximation outlined in Moore et al. (2016), who show that the eccentricity as a function of frequency can be calculated analytically to 3PN order if the eccentricity is assumed to be small (better than 2% at $e = 0.1$ for low frequencies $\lesssim 200$ Hz):

$$e_t = e_0 \left(\frac{\xi \phi_0}{\xi \phi} \right)^{\frac{19}{18}} \frac{\epsilon(\xi \phi)}{\epsilon(\xi \phi_0)}, \quad (1)$$

where

$$\xi \phi = (m_1 + m_2) \pi f_{\text{GW}}, \quad (2)$$

is a dimensionless frequency parameter, which serves as the PN expansion parameter, and $\epsilon(\xi \phi)$ is a 3PN correction term. From this (1) becomes, at 0th order, in the $e \rightarrow 0$ limit:

$$e_t(f_{\text{GW}}) \approx e_0 \left(\frac{f_{\text{GW}_t}}{f_{\text{GW}_0}} \right)^{-19/18}. \quad (3)$$

We use this equation to trace out the e_{10} path from f_{ref} to 10 Hz. As we move along the e_{10} path, we vary ω_{ref} —our indirect estimate of the reference argument of periapsis. By studying how the waveform changes for different values of ω_{ref} along the e_{10} path, we can assess the affect of the argument of periapsis on gravitational-wave inference.

The waveform overlap (Flanagan & Hughes 1998) describes the similarity between two gravitational waveforms. By calculating the overlap between waveforms that are the same in all parameters besides the argument of periapsis, we can quantify the amount ω_{ref} changes the waveforms. The phase and time maximised overlap is given by

$$O = \max(\phi_0, t_0) \frac{\langle h_1 | h_2 \rangle}{\sqrt{\langle h_1 | h_1 \rangle \langle h_2 | h_2 \rangle}}, \quad (4)$$

where $\langle a | b \rangle$ is the inner product defined such that

$$\langle a | b \rangle = 4 \text{Re} \int_0^\infty df \frac{\tilde{a}(f) \tilde{b}(f)}{S_h(f)}, \quad (5)$$

where $S_h(f)$ is the power spectral density of the noise. We calculate the overlap over a grid of waveforms generated with TEOBResumS and SEOBNRE, corresponding to the predicted change in eccentricity and frequency over an orbital cycle.

We generate the reference waveform with the parameters listed in Table 1. The overlap $O = 1$ when the reference waveform and comparison waveform are the same. We calculate the overlap (maximized over phase and time) on a grid of $(e_{\text{ref}}, f_{\text{ref}})$. Each grid-space records the overlap between a waveform with $(e_{\text{ref}}, f_{\text{ref}})$ and the fiducial waveform at $e_{\text{fiducial}} = 0.1$, $f_{\text{fiducial}} = 10$ Hz. This is shown in Fig. 2 along with the e_{10} path. The effective argument of periapsis ω_{eff} parameterises the location along the e_{10} path and our measurement of ω_{ref} . We assume that ω_{eff} values are evenly spaced along the curve and that $\omega_{\text{eff}} = 0$ when $e_{\text{ref}}, f_{\text{ref}} = e_{\text{fiducial}}, f_{\text{fiducial}}$. In reality ω_{ref} at the fiducial waveform is arbitrary. The waveform overlap

¹ Comparing the eccentricities of the two waveforms is not straightforward, since they employ different definitions of eccentricity and its evolution with frequency. We ignore this added complication for this study, however future work should consider how eccentricity values map to each other in different waveforms. This is under development by Kneee et al. (2022).

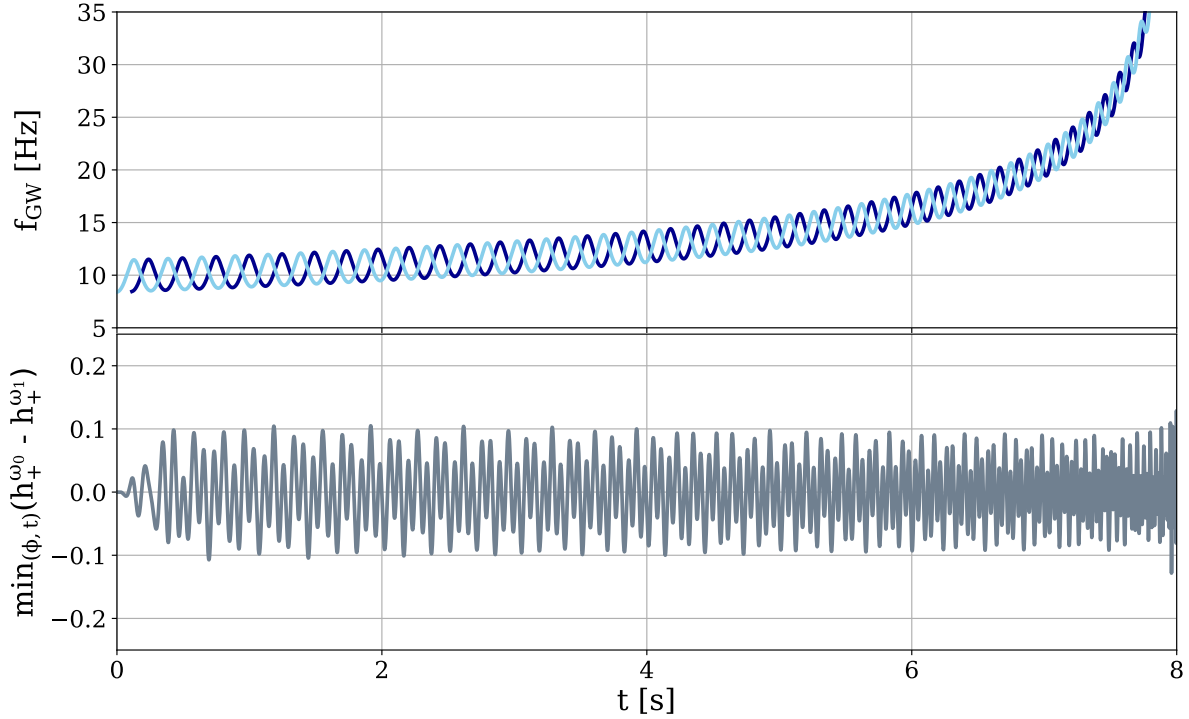


Figure 1. The effect of changing the reference argument of periaapsis ω_{ref} on the gravitational waveforms for a GW150914-like event with parameters listed in Table 1. Top panel: the frequency evolution of a binary black hole inspiral of $f_{\text{ref}} = 10$ Hz, $e_{\text{ref}} = 0.1$ and $f_{\text{ref}} = 9.95$ Hz, $e_{\text{ref}} = 0.1005$. This corresponds to a change in ω_{ref} of $\approx \pi$. It can be thought of as the system being evolved back in time by half a waveform cycle and illustrates the way waveforms change when they have different values of ω_{ref} . The peaks and troughs show the periaapsis and apoapsis passages respectively. The change in frequency in one waveform cycle is approximated as the difference in frequency between two troughs. Bottom Panel: The difference between the waveforms plotted in the top panel, minimised over phase and time.

Table 1. Injection parameters of the fiducial waveform used to calculate the grid of overlaps and likelihood of ω_{ref} using `TEOBResumS`. The parameters are chosen to be similar to GW150914, but the distance increased such that the SNR ≈ 17 at design sensitivity.

Parameter	Abbreviation	Value
black hole masses	m_1, m_2	30, 25 M_\odot
reference eccentricity	e_{fiducial}	0.1
reference frequency	f_{fiducial}	10 Hz
spin parameters	χ_1, χ_2	0.0
inclination	θ_{JN}	0.6
phase	ϕ_c	1.5
luminosity distance	D_L	1419 Mpc
right ascension	RA	3.5
declination	Dec	0.5

follows a sinusoidal pattern and reaches a minimum of ≈ 0.95 at $\omega_{\text{eff}} \approx \pi$. This is expected because when $\omega_{\text{eff}} = 2\pi$, the waveforms are the same but initialised one cycle apart, resulting in a local maximum for the waveform overlap. Our change in overlap does not match that of Islam et al. (2021), potentially because we used LVK noise, rather than white noise. This suggests that ω_{ref} is less resolvable in realistic (noisy) gravitational-wave data.

Two waveforms with different reference arguments of periaapsis (but otherwise identical parameters) can be distinguished from the

reference waveform if (Lindblom et al. 2008; Baird et al. 2013):

$$1 - \mathcal{O} \sim \text{SNR}^{-2}, \quad (6)$$

where $\text{SNR} = \sqrt{\langle h_0 | h_0 \rangle}$ is the optimal matched-filter SNR of the reference waveform h_0 . Hence, for the lowest value of the overlap in Fig. 2 of ≈ 0.95 , an SNR of ≈ 5 is required to distinguish this waveform from the reference waveform. Of course, this assumes that all other parameters are known perfectly, which is not the case for real inference calculations in noisy data. In the subsequent section, we determine the extent to which ω_{ref} can be resolved in noisy data.

3 METHOD

We calculate the posterior distribution for ω_{ref} for a simulated eccentric gravitational-wave signal. Table 1 shows the injection parameters of the chosen eccentric fiducial waveform. We choose the system to have a relatively loud but realistic SNR of ≈ 17 . The first step is to generate standard posterior samples at a fixed value of f_{ref} . To this end, we carry out parameter estimation using the Bayesian Inference Library (Bilby) and the `bilby_pipe` pipeline (Ashton et al. 2019; Romero-Shaw et al. 2020a), the spin-aligned eccentric waveform approximant `TEOBResumS` (Chiamello & Nagar 2020) and the nested

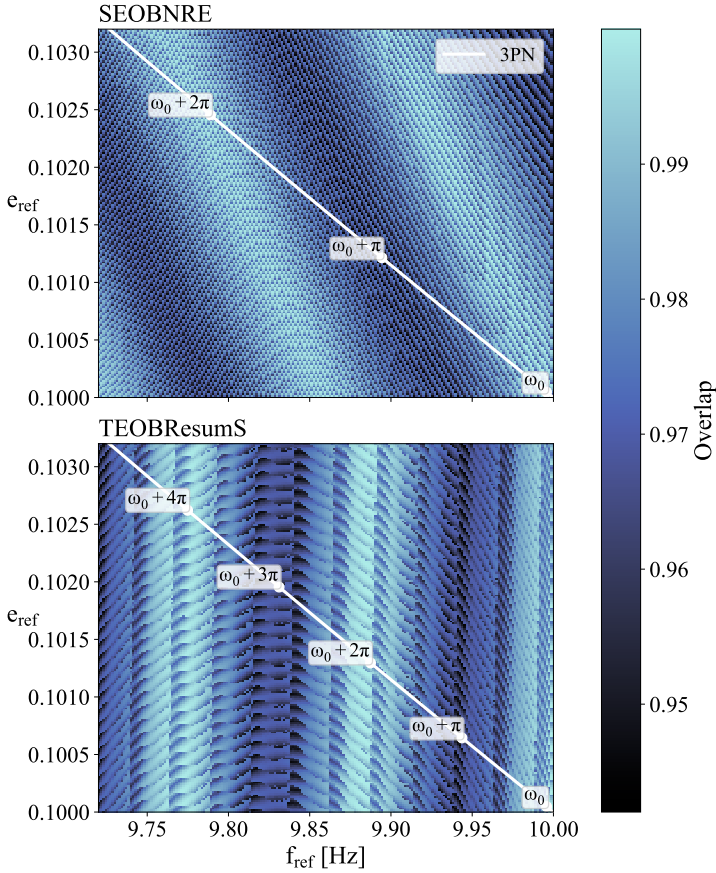


Figure 2. The maximised overlap over approximately two waveform periods. Top panel: SEOBNRE. Bottom panel: TEOBResumS. The white line shown is the 3PN expansion, showing the evolution of a system starting at the fiducial waveform, labelled as ω_0 in the bottom right corner. The overlap varies by about 0.05 throughout the waveform cycle, suggesting that ω_{ref} has a non-negligible effect on the waveforms.

sampler *dynesty* (Speagle 2019).² We also generate posterior samples with SEOBNRE (Cao & Han 2017) for an injection with similar parameters to TEOBResumS.³ We use the LIGO amplitude spectral density noise curves at design sensitivity.⁴ We use uniform priors in the component masses, spins, luminosity distance and eccentricity.⁵ The initial posterior samples from this step are all (inadvertently) assigned some *implicit* argument of periaapsis ω_{fixed} , which is completely determined by $(e_{\text{ref}}, f_{\text{ref}})$. In this sense, ω_{ref} is not a free parameter of the initial posterior samples.

The next step is to importance sample the initial posterior samples in order to obtain the results we would have obtained if ω_{ref} had been

a free parameter. For each sample i , we calculate a weight

$$w(\theta_i|d) = \frac{\int d\omega \mathcal{L}(d|\theta_i, \omega) \pi(\omega)}{\mathcal{L}(d|\theta_i, \omega_{\text{fixed}})}. \quad (7)$$

The numerator of the weight is the “target likelihood” that marginalises over ω_{ref} while the denominator is the “proposal likelihood” used to generate the initial samples.⁶ The numerator integral over ω_{ref} is along the e_{10} path described above. Next, for each sample i , we calculate the posterior probability density for ω_{ref} given parameters θ_i : $p(\omega|d, \theta_i)$; see the light blue traces in Fig. 3, which are proportional to $\ln p(\omega|d, \theta_i)$. We use the weights $w(\theta_i|d)$ and the posteriors $p(\omega|d, \theta_i)$ to calculate the posterior probability density of ω_{ref} given the data:

$$\begin{aligned} p(\omega|d) &\propto \pi(\omega) \mathcal{L}(d|\omega) \\ &\propto \int d\theta \mathcal{L}(d|\theta, \omega) \pi(\theta) \\ &\propto \int d\theta \pi(\theta) \left(\frac{\mathcal{L}(d|\theta, \omega)}{\mathcal{L}(d|\theta, \omega_{\text{fixed}})} \right) \mathcal{L}(d|\theta, \omega_{\text{fixed}}) \\ &\propto \int d\theta \pi(\theta) \left(\frac{p(\omega|d, \theta) \int d\omega' \mathcal{L}(d|\theta, \omega')}{\mathcal{L}(d|\theta, \omega_{\text{fixed}})} \right) \mathcal{L}(d|\theta, \omega_{\text{fixed}}) \\ &\propto \int d\theta p(\omega|d, \theta) w(\theta|d) \left(\pi(\theta) \mathcal{L}(d|\theta, \omega_{\text{fixed}}) \right) \\ &\propto \sum_i p(\omega|d, \theta_i) w(\theta_i|d) \end{aligned} \quad (8)$$

In this derivation we implicitly assume a uniform prior for ω_{ref} . In the final line, the posterior is written as a sum over initial samples. Graphically, this implies that the posterior for ω_{ref} is a weighted average of the (exponential of the) light blue curves in Fig. 3.

4 RESULTS AND DISCUSSION

Figure 3 shows the posterior distribution for ω_{eff} —our parameterisation for ω_{ref} , calculated with TEOBResumS. We plot the results for the fiducial waveform shown in Table 1 compared to the posterior obtained from a louder, $\text{SNR} \approx 30$ signal. The marginalised \ln -likelihood changes by ≈ 0.7 over the waveform cycle for the low-SNR injection. One rule of thumb states that a feature is strongly resolved if it is measured with a \ln -likelihood of 8. With that threshold, our result indicate that we do not confidently resolve the argument of periaapsis for this injection at $\text{SNR} \approx 17$. At $\text{SNR} \approx 30$, the \ln -likelihood changes by ≈ 15 . This suggests that ω_{eff} is strongly resolved for this simulation. Figure 3 (bottom panel) shows the posterior distribution for ω_{eff} . The shape of the distribution suggests that $\omega_{\text{eff}} \approx 0 \pm \pi/2$ is slightly favoured by the data at $\text{SNR} \approx 17$ and strongly favoured at $\text{SNR} \approx 30$. The width of the peak is comparable to the prior volume. This means that while the data has found some preference for the value of ω_{eff} , at $\text{SNR} \approx 17$, it is not well constrained and is only slightly more informative than the prior probability distribution. At $\text{SNR} \approx 30$, the peak becomes narrower and rules out more of the prior volume - increasing the confidence of the measurement. As the SNR increases, the unfaithfulness of waveforms from numerical relativity simulations becomes more detectable along with ω_{ref} . The mismatch from numerical relativity at $e \approx 0.1$ is $\approx 1\%$ (Chiaramello

² We implement the speed-up trick described in O’Shea & Kumar (2021), where the integrator error tolerances are loosened slightly. This modification allows full parameter estimation to be performed directly with TEOBResumS.

³ SEOBNRE samples are generated by performing likelihood reweighting (Payne et al. 2019) on samples generated with the fast quasi-circular waveform IMRPhenomD (Khan et al. 2016). This has the disadvantage of reducing the number of effective posterior samples.

⁴ amplitude spectral density curves are taken from <https://dcc.ligo.org/LIGO-T2000012/public> (Abbott et al. 2018)

⁵ We sample with 1000 live points, phase and time marginalisation turned on and a stopping criterion of $\Delta \log \mathcal{Z} < 0.1$, where \mathcal{Z} is the Bayesian evidence.

⁶ When calculating the weight in Eq. 7, both likelihoods are implicitly marginalised over the time and phase of coalescence.

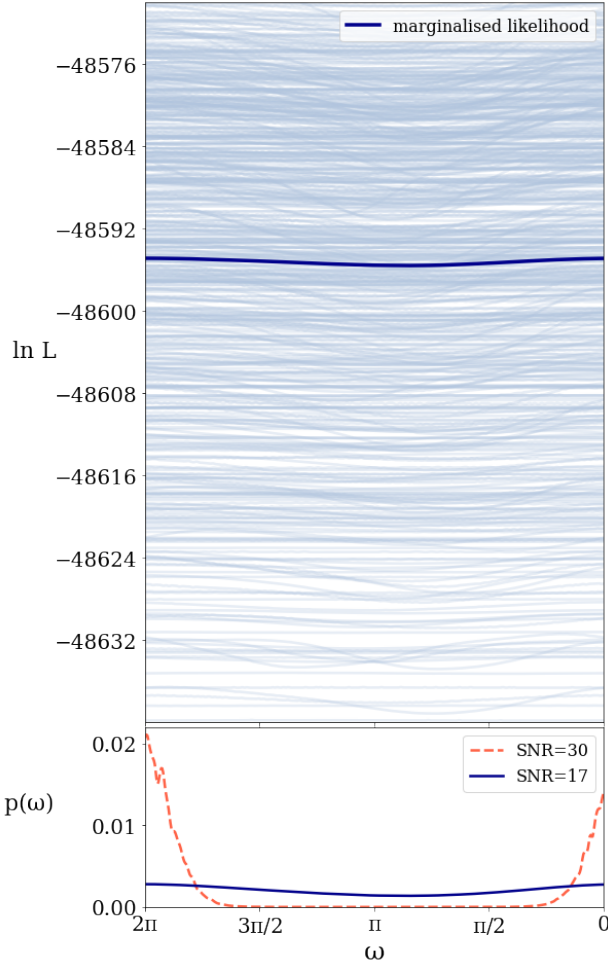


Figure 3. The argument of periaapsis measured with TEOBResumS. Top: The likelihood over ω_{eff} , plotted for 1000 posterior samples generated with TEOBResumS, with the averaged log likelihood highlighted in dark blue. Some of the curves appear almost completely straight, corresponding to posterior samples with eccentricity close to zero. Bottom: In dark blue is the posterior distribution over the same parameter space. In dashed red is shown the posterior obtained with the same injection but at SNR (≈ 30). The width of the peaks of the distributions provide an indication of how well we can resolve ω_{eff} . ω_{eff} is only just beginning to become resolvable at SNR ≈ 17 but is highly resolvable at SNR ≈ 30 .

& Nagar 2020), which is less than the mismatch caused by ω_{ref} in Section 2. Hence, ω_{ref} is likely to be more important than waveform systematics at the SNR and eccentricities considered here.

We repeat the SNR ≈ 17 analysis with SEOBNRE and present an analogous version of Fig. 3, shown in Fig. 4. The results are similar to and consistent with those obtained using TEOBResumS ($\Delta \ln(\mathcal{L}) \approx 1.3$), and support the evidence that ω_{eff} is not strongly resolvable in current eccentric gravitational-wave events. The posterior obtained contains less low-eccentricity samples, which is likely why ω_{eff} seems slightly more resolved in this injection. The traces along the e_{10} path are much noisier than for TEOBResumS, producing a marginalised likelihood and posterior for ω_{eff} that is less smooth. Another difference between the results is that the SEOBNRE data prefer $\omega_{\text{eff}} \approx \pi \pm \pi/2$ which suggests the arbitrary reference argument of periaapsis set by the fiducial waveform ($e_{\text{fiducial}} = 0.1$, $f_{\text{fiducial}} = 10$ Hz) is out of phase by π between the waveforms. The discrepancy is thought to be due to differences in the waveform systematics between the waveform models. In particular, in SEOBNRE, the reference eccentricity is subject to a corrective transform according to the reference eccentricity before constructing the waveform, which means

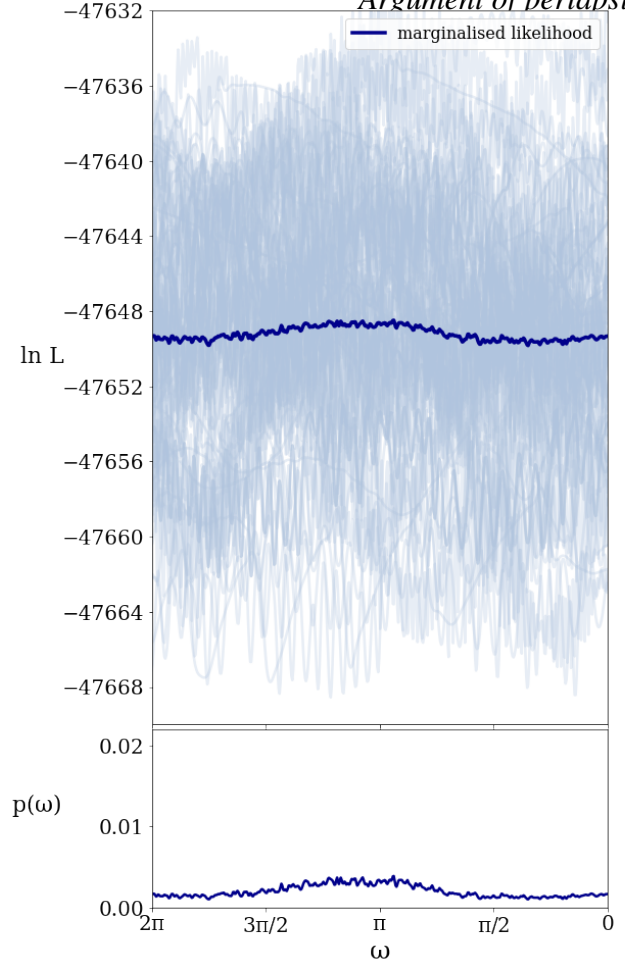


Figure 4. The argument of periaapsis measured with SEOBNRE. Top: The likelihood over ω_{eff} , calculated using the waveform SEOBNRE. The average is highlighted in dark blue. The \ln -likelihood changes by ≈ 1.3 , higher than for TEOBResumS partly because of the noisy quality of the result. This result suggests that ω_{eff} can not be resolved in the data of eccentric binary black hole mergers at the SNR shown here (≈ 17). Bottom: The posterior distribution for ω_{eff} over the parameter space. The posterior is noisier but more peaked than the TEOBResumS result but has a similar width.

that the waveforms generated might not follow the intended e_{10} path. For more details on eccentric waveform systematics, see Varma & Pfeiffer, in prep, Knee et al., in prep.

There is a universal probability density function for the distribution of SNR for a population of binary black holes (Schutz 2011; Chen & Holz 2014), given by

$$f_{\rho} = \frac{3\rho_{\text{min}}^3}{\rho^4}, \quad (9)$$

where ρ_{min} is the threshold SNR for a detection, assumed to be 12 for a 3-detector network. Hence, only ~ 6 percent of events will be louder than SNR $\gtrsim 30$. Since only ~ 5 percent of mergers are expected to be eccentric at 10 Hz if dynamical assembly is the dominant formation channel (e.g., Samsing & Ramirez-Ruiz 2017; Samsing 2018; Samsing & D’Orazio 2018; Zevin et al. 2020), this means that ω_{ref} will not be measurable in the vast majority of binary black holes with the current detector configuration. However, improved detector sensitivity and detection rates should mean that even 6 percent of eccentric events could become a substantial population, for which ω_{ref} should not be neglected.

The complexity of stellar evolution and star cluster physics have made it difficult to predict the dominant binary black hole formation

channels and distinguish them in gravitational-wave data. The orbital eccentricity of these systems is an important marker of the formation channels. However, to accurately infer the parameters of eccentric binaries, we need to consider the argument of periapsis, which is not inferred through parameter estimation currently.

In this work, we find that ω_{ref} is only just beginning to become resolvable for a moderately eccentric binary black hole system (with parameters similar to GW150914) when the SNR exceeds approximately 17. By $\text{SNR} \approx 30$, ω becomes very well resolvable for the same system parameters. Given the modest SNR of current eccentric candidates (GW190521 was detected with $\text{SNR} \approx 15$), past analyses that fix ω_{ref} to an arbitrary value are unlikely to suffer from significant systematic error. However, as the gravitational-wave transient catalog grows, and more events are detected with higher SNR, it will soon become important to include the argument of periapsis in parameter estimation analyses. Future studies should consider marginalising over ω_{ref} to avoid introducing bias to the results.

At least four events in the current gravitational-wave transient catalogue may contain traces of eccentricity, including GW190521, GW190620_030421 (Romero-Shaw et al. 2020b; Romero-Shaw et al. 2021; Gayathri et al. 2022), GW191109_010717, GW200208_222617 (Romero-Shaw et al. 2022 (in prep)), GW151226 and GW170608 (Wu et al. 2020; O’Shea & Kumar 2021). We show that if these events are eccentric, the reference ω of these systems is not resolvable. Therefore, it is likely that previous analyses that have not marginalized over ω_{ref} have results that are robust to changes in ω_{ref} . Our recipe indirectly varies ω_{ref} by simultaneously adjusting e_{ref} and f_{ref} . In the long-term, the only solution is to build waveform approximants that allow users to vary ω_{ref} directly.

5 ACKNOWLEDGEMENTS

This work is supported through Australian Research Council (ARC) Centre of Excellence CE170100004, and Discovery Project DP220101610. T. A. C. receives support from the Australian Government Research Training Program. I.M.R.-S. acknowledges support received from the Herchel Smith Postdoctoral Fellowship Fund. Computing was performed using the LIGO Laboratory computing cluster at California Institute of Technology, and the OzSTAR Australian national facility at Swinburne University of Technology.

6 DATA AVAILABILITY

The data underlying this article will be shared on reasonable request to the corresponding author.

REFERENCES

Aasi J., et al., 2015, *Classical and Quantum Gravity*, 32, 074001
 Abbott B. P., et al., 2017, *Phys. Rev. Lett.*, 119, 161101
 Abbott B. P., et al., 2018, *Living Rev. Rel.*, 21, 3
 Abbott B. P., et al., 2019, *Phys. Rev. X*, 9, 031040
 Abbott R., et al., 2020a, *Phys. Rev. Lett.*, 125, 101102
 Abbott B. P., et al., 2020b, *ApJ*, 892, L3
 Abbott R., et al., 2021a, arXiv e-prints, p. arXiv:2111.03606
 Abbott R., et al., 2021b, arXiv e-prints, p. arXiv:2111.03634
 Abbott R., et al., 2021c, *Phys. Rev. X*, 11, 021053
 Abbott R., Abbott T. D., Abraham S., Acernese F., Ackley K., Adams A., Adams C., et al., 2021d, *ApJ*, 913, L7
 Abbott R., et al., 2021e, *ApJ*, 915, L5
 Acernese F., et al., 2015, *Class. Quant. Grav.*, 32, 024001

Akutsu T., et al., 2020, *Progress of Theoretical and Experimental Physics*, 2021
 Ashton G., et al., 2019, *Astrophys. J. Suppl.*, 241, 27
 Baird E., Fairhurst S., Hannam M., Murphy P., 2013, *Phys. Rev. D*, 87, 024035
 Belczynski K., Holz D. E., Bulik T., O’Shaughnessy R., 2016, *Nature*, 534, 512
 Bethe H. A., Brown G. E., 1998, *Astrophys. J.*, 506, 780
 Buonanno A., Damour T., 1999, *Phys. Rev. D*, 59
 Busicchio R., Klein A., Roebber E., Moore C. J., Gerosa D., Finch E., Vecchio A., 2021, *Phys. Rev. D*, 104, 044065
 Cao Z., Han W.-B., 2017, *Phys. Rev. D*, 96, 044028
 Chen H.-Y., Holz D. E., 2014, arXiv e-prints, p. arXiv:1409.0522
 Chiamello D., Nagar A., 2020, *Phys. Rev. D*, 101, 101501
 Flanagan E. E., Hughes S. A., 1998, *Phys. Rev. D*, 57, 4566
 Gayathri V., et al., 2022, *Nature Astronomy*, 6, 344
 Gröbner M., Ishibashi W., Tiwari S., Haney M., Jetzer P., 2020, *A&A*, 638, A119
 Huerta E., et al., 2014, *Phys. Rev. D*, 90
 Islam T., et al., 2021, *Phys. Rev. D*, 103, 064022
 Khan S., Husa S., Hannam M., Ohme F., Pürrer M., Forteza X. J., Bohé A., 2016, *Phys. Rev. D*, 93, 044007
 Klein A., 2021, arXiv e-prints, p. arXiv:2106.10291
 Knee A., et al., 2022, in prep
 Lindblom L., Owen B. J., Brown D. A., 2008, *Phys. Rev. D*, 78, 124020
 Liu X., Cao Z., Shao L., 2020, *Phys. Rev. D*, 101, 044049
 Lower M. E., Thrane E., Lasky P. D., Smith R., 2018, *Phys. Rev. D*, 98, 083028
 Mandel I., Farmer A., 2022, *Physics Reports*, 955, 1
 Moore B., Favata M., Arun K., Mishra C. K., 2016, *Physical Review D*, 93
 Nagar A., et al., 2018, *Phys. Rev. D*, 98, 104052
 Nagar A., Pratten G., Riemenschneider G., Gamba R., 2020, *Phys. Rev. D*, 101, 024041
 O’Leary R. M., Rasio F. A., Fregeau J. M., Ivanova N., O’Shaughnessy R. W., 2006, *Astrophys. J.*, 637, 937
 O’Leary R. M., Kocsis B., Loeb A., 2009, *MNRAS*, 395, 2127
 O’Shea E., Kumar P., 2021, arXiv e-prints, p. arXiv:2107.07981
 Payne E., Talbot C., Thrane E., 2019, *Phys. Rev. D*, 100, 123017
 Peters P. C., 1964, *Phys. Rev.*, 136, B1224
 Rodriguez C. L., Chatterjee S., Rasio F. A., 2016, *Phys. Rev. D*, 93, 084029
 Rodriguez C. L., Amaro-Seoane P., Chatterjee S., Kremer K., Rasio F. A., Samsing J., Ye C. S., Zevin M., 2018, *Phys. Rev.*, D98, 123005
 Romero-Shaw I. M., Lasky P. D., Thrane E., 2019, *Mon. Not. Roy. Astron. Soc.*, 490, 5210
 Romero-Shaw I. M., et al., 2020a, *Mon. Not. Roy. Astron. Soc.*, 499, 3295
 Romero-Shaw I. M., Lasky P. D., Thrane E., Bustillo J. C., 2020b, *Astrophys. J. Lett.*, 903, L5
 Romero-Shaw I., Lasky P. D., Thrane E., 2021, *ApJ*, 921, L31
 Romero-Shaw I., et al., 2022, in prep
 Samsing J., 2018, *Phys. Rev. D*, D97, 103014
 Samsing J., D’Orazio D. J., 2018, *Mon. Not. Roy. Astron. Soc.*, 481
 Samsing J., Ramirez-Ruiz E., 2017, *The Astrophysical Journal*, 840, L14
 Schutz B. F., 2011, *Classical and Quantum Gravity*, 28, 125023
 Speagle J. S., 2019, arXiv e-prints, p. arXiv:1904.02180
 Stevenson S., Vigna-Gómez A., Mandel I., Barrett J. W., Neijssel C. J., Perkins D., de Mink S. E., 2017, *Nature Communications*, 8, 14906
 Wu S., Cao Z., Zhu Z.-H., 2020, *MNRAS*, 495, 466
 Yang Y., Bartos I., Haiman Z., Kocsis B., Márka Z., Stone N. C., Márka S., 2019, *apj*, 876, 122
 Yun Q., Han W.-B., Zhong X., Benavides-Gallego C. A., 2021, *Phys. Rev. D*, 103, 124053
 Zevin M., et al., 2020, arXiv e-prints, p. arXiv:2011.10057
 Zevin M., Romero-Shaw I. M., Kremer K., Thrane E., Lasky P. D., 2021, arXiv e-prints, p. arXiv:2106.09042